Role of target shell structure in direct reactions involving weakly bound ^{7}Li

S. K. Pandit,[1,2,*] A. Shrivastava,[1,2] K. Mahata,[1,2] V. V. Parkar,[1] N. Keeley,[3] P. C. Rout,[1,2] K. Ramachandran,[1] C. S. Palshetkar,[1] I. Martel,[4] A. Kumar,[1] A. Chatterjee,[1] and S. Kailas[1,†]

[1]*Nuclear Physics Division, Bhabha Atomic Research Centre, Mumbai 400085, India*

[2]*Homi Bhabha National Institute, Anushaktinagar, Mumbai 400094, India*

[3]*National Centre for Nuclear Research, ul. Andrzeja Sołtana 7, 05-400 Otwock, Poland*

[4]*Science and Technology Research Center, University of Huelva, E-21071 Huelva, Spain*

(Received 19 March 2019; revised manuscript received 4 June 2019; published 29 July 2019)

The effect of the shell structure of the target nuclei (^{89}Y and ^{93}Nb) on reaction mechanisms involving the weakly bound ^{7}Li projectile has been investigated via a comparative study of different processes. Measurements of direct breakup, nucleon transfer leading to the ejectile in bound as well as unbound states, and elastic scattering have been carried out for the ^{7}Li + ^{89}Y system at three different energies near the Coulomb barrier. An extensive analysis of this comprehensive data set was carried out using coupled channel calculations and compared with a previous similar study for the ^{7}Li + ^{93}Nb system. The observed cross sections at low target excitations for nucleon transfer reactions correlate with the vacancies in the valance orbitals.

DOI: 10.1103/PhysRevC.100.014618

I. INTRODUCTION

Reactions involving strongly bound nuclei are greatly influenced by the coupling of various internal degrees of freedom (transfer, inelastic excitation) with the relative motion [1]. Also, for weakly bound nuclei it is crucial to understand the effect of couplings due to low-lying continuum states [2–4]. From the measurement point of view, the challenging task is to disentangle various breakup processes, e.g., direct breakup or nucleon transfer followed by breakup of the ejectile (transfer breakup). Hence, exclusive measurements are required for the deconvolution of different channels. Moreover, theoretical modeling of the influence of all possible excited states of projectile (ejectile) and target (residue) nuclei in a coherent way is also difficult. There are limited exclusive measurements having data on absolute cross sections [5–14]. Further, there are no quantitative studies available on the role of the structure of the target nucleus on different processes.

In our earlier work, various breakup processes were studied in the ^{7}Li + ^{93}Nb system via exclusive measurements and theoretical analyses based on the coupled channel framework [11,12]. There are one valence proton and two valance neutrons in ^{93}Nb, with respect to semimagic ^{90}Zr. The present work aims to understand the role of target structure in the mechanism of reactions involving weakly bound projectiles. New measurements have been carried out for ^{89}Y, which has a closed neutron shell and a single proton hole. A comparative study of 1n-stripping and 1p-pickup channels for the ^{7}Li + ^{89}Y, ^{93}Nb systems will be useful to understand the influence of the shell structure of the target and target-like nuclei on the breakup processes following nucleon transfer.

This paper reports the simultaneous measurement of absolute angular distributions for both 1p pickup and 1n stripping followed by breakup of the ejectile as well as direct breakup of the projectile. Angular distributions for elastic scattering and nucleon transfer to bound states have also been measured. Coupled channels Born approximation (CCBA) and continuum discretized coupled channel (CDCC) calculations which explain the large number of observables are presented. A comparative study of these processes for ^{89}Y and ^{93}Nb targets has also been carried out to probe the influence of the shell structure of the target nuclei on the reaction mechanism.

The paper is organized as follows: experimental details are given in Sec. II. The analysis and results are presented in Sec. III. Details of the coupled channel calculations are described in Sec. IV. The role of the shell structure of the target nuclei on different processes is discussed in Sec. V followed by a summary and conclusions in Sec. VI.

II. EXPERIMENTAL DETAILS

The experiment was performed at the BARC-TIFR Pelletron-Linac facility, Mumbai, with ^{7}Li beams of energies 23, 28, and 30 MeV. A self-supporting ^{89}Y foil of thickness $\approx$2 mg/cm^2 was used as the target. Use of segmented large-area Si detectors served the requirements of high granularity to detect low-lying resonant states and large solid angle to measure low cross sections. Two telescopes consisting of segmented Si detectors of active area 5 × 5 cm^2 were used in the experiment. The thicknesses of the ΔE and E detectors were 50 μm and 1.5 mm, respectively. While the ΔE detectors were single sided with 16 strips on the front face, the E detectors were double sided with 16 strips each on the front and rear faces. The detected relative angles between the two

*sanat@barc.gov.in

†Present address: Manipal Centre for Natural Sciences, Manipal University, Manipal 576104, India.

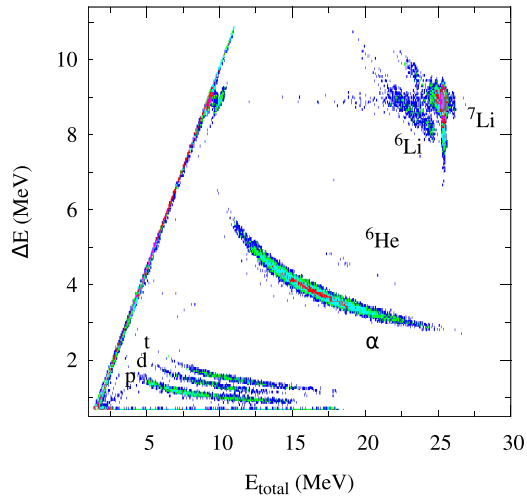

FIG. 1. Typical particle identification spectrum of ΔE vs $E_{\rm tot}$ for the ^{7}Li + ^{89}Y system at $E_{\rm lab} = 27.7$ MeV, $\theta_{\rm lab} = 60^{\circ}$.

fragments ranged from 1° to 24°. Further details of the setup are already given in Refs. [11,15]. Measurements were carried out at different angle settings to cover a total angular range of 30°–130° around the grazing angle. As the singles counting rate was estimated to be too high for the strip detectors to handle, three Si surface-barrier detector telescopes (thicknesses $\Delta E \approx 20$–50 μm, $E \approx 450$–1000 μm) were used for the measurements of the elastic scattering angular distributions at forward angles. Two Si surface-barrier detectors (thickness ≈300 μm) were kept at ±20° for absolute normalization. The detectors were calibrated using the known α energies from a ^{239}Pu-^{241}Am source and the ^{7}Li + ^{12}C reaction at 23 MeV.

III. ANALYSIS AND RESULTS

Detected particles were identified using the energy loss information in the ΔE and E detectors. A typical particle identification spectrum of ΔE vs $E_{\rm tot}$ for the ^{7}Li + ^{89}Y system is shown in Fig. 1. The scattering angles (θ, ϕ) of the detected fragments with respect to the beam direction were determined from the positions of the vertical and horizontal strips being fired in the double-sided E detectors. Detected particles were tagged by kinetic energy (E), mass number (A) and scattering angle (θ, ϕ). The energy and scattering angle were converted from the laboratory frame to the c.m. frame of the target-projectile system in event-by-event mode. The pairs of particles observed in the coincident events were α-α, α-d, and α-t. The α-α event rate was found to be highest while the α-t rate was lowest. The angle of the ejectile ($\theta_{\rm ejectile}$) prior to breakup and relative angles ($\theta_{\rm rel}$) between the fragments were calculated from the measured scattering angles (θ_1, ϕ_1; θ_2, ϕ_2). The relative energies ($E_{\rm rel}$) between the fragments were calculated from their masses (A_1, A_2), kinetic energies (E_1, E_2), and $\theta_{\rm rel}$ values. Correlation plots of the energy of the α particle, E_α, vs the relative energies $E_{\alpha\alpha}$, $E_{\alpha d}$, and $E_{\alpha t}$ are shown in Figs. 2(a), 2(b), and 2(c), respectively, for $E_{\rm lab} = 27.7$ MeV, $\theta_{\rm ejectile} = 55^{\circ}$–$65^{\circ}$. The corresponding projections of the relative energy are shown in the right panels (d), (e), and (f) of the figure. The excitation energy of the ejectile prior to

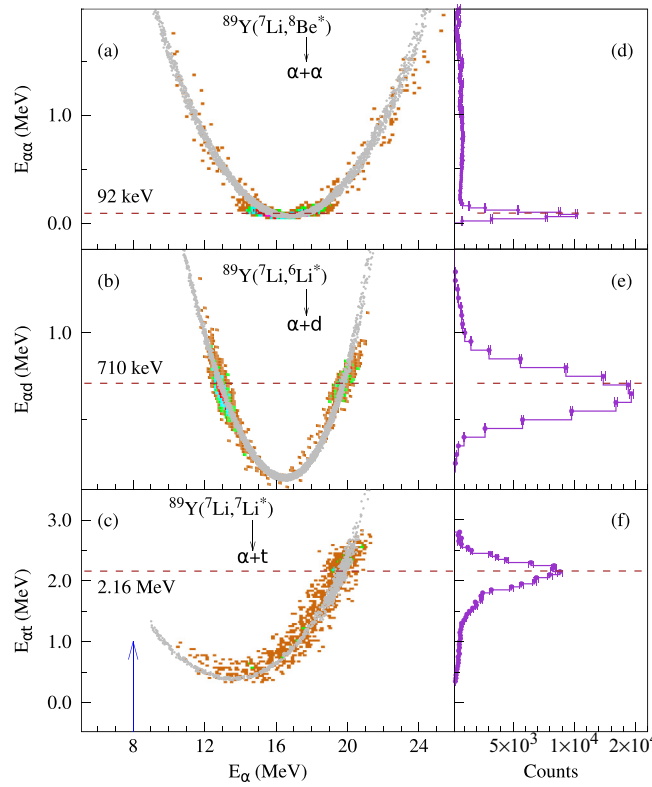

FIG. 2. Measured energy correlations of fragments in breakup of (a) ^{8}Be* ($1p$ pickup), (b) ^{6}Li* ($1n$ stripping), and (c) ^{7}Li* at $E_{\rm lab} = 27.7$ MeV, $\theta_{\rm ejectile} = 55^{\circ}$–$65^{\circ}$, corresponding to $\theta_{\rm rel}^{\alpha\alpha} = 3^{\circ}$, $\theta_{\rm rel}^{\alpha d} = 10^{\circ}$, and $\theta_{\rm rel}^{\alpha t} = 15^{\circ}$, respectively. The arrow on the x axis indicates the detection threshold. The kinematical curves obtained from the Monte Carlo simulation are shown by gray shading. The projections of the relative energy distribution are shown in the corresponding right panels: (d), (e), and (f).

breakup was obtained by adding the breakup threshold to the measured $E_{\rm rel}$. The peaks in the relative energy spectra of $E_{\alpha\alpha}$, $E_{\alpha d}$, and $E_{\alpha t}$ at 92 keV, 710 keV and 2.16 MeV correspond to the breakup of ^{8}Be (g.s.), ^{6}Li (3_1^+, 2.18 MeV) and ^{7}Li ($\frac{7}{2}^-$, 4.63 MeV), respectively. The coincidence detection efficiency of the setup for the different breakup processes was estimated accurately using a Monte Carlo simulation procedure [15].

Typical excitation energy spectra of the target-like nuclei, obtained using the missing energy technique, for $1p$ pickup and $1n$ stripping for the ^{7}Li + ^{89}Y system are presented in Figs. 3(a) and 3(b), respectively. The excitation energy spectrum of ^{89}Y corresponding to both prompt (i.e., nonresonant) and resonant breakup of ^{7}Li is shown in Fig. 3(c). For comparative purposes, spectra for the same processes for the ^{7}Li + ^{93}Nb system, measured in an earlier work [11], are also shown in the right panel of the figure. According to the semiclassical theory, the excitation energy spectra are expected to peak around $E^* = Q_{\rm gg} - Q_{\rm opt}$ for transfer reactions [16,17]. Here $Q_{\rm gg}$ and $Q_{\rm opt}$ are the ground state and optimum Q values, respectively. Large populations of states around 3.5 MeV for $1p$ pickup (^{92}Zr and ^{88}Sr) and the ground state for $1n$ stripping (^{94}Nb and ^{90}Y) are in agreement with the semiclassical theory.

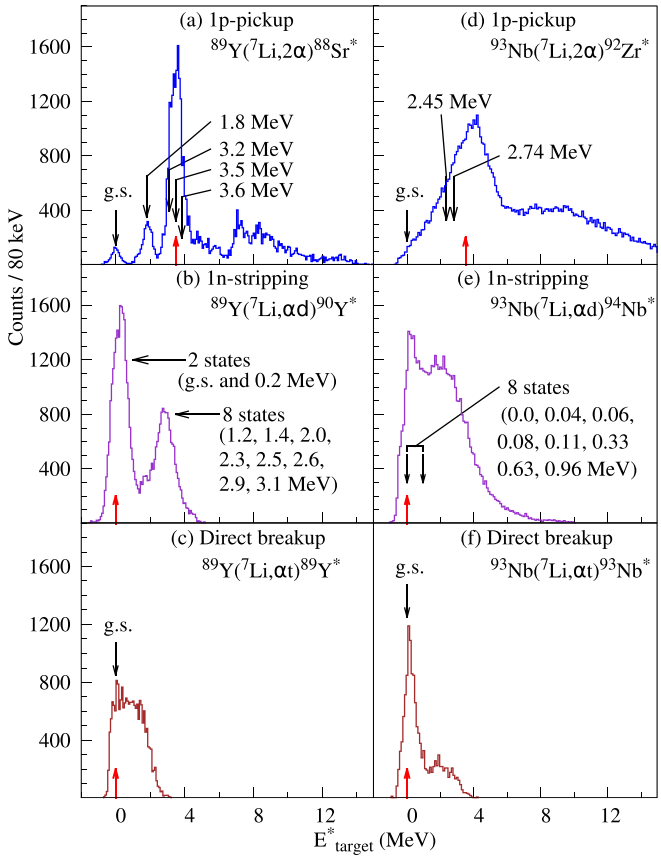

FIG. 3. Measured excitation energy spectra of target-like products for the ^{7}Li + ^{89}Y, ^{93}Nb reactions at $E_{\rm lab} = 27.7$ MeV. The upward arrows indicate the position of $E^* = Q_{\rm gg} - Q_{\rm opt}$. States included in the coupled channel calculations are indicated. Details are given in the text.

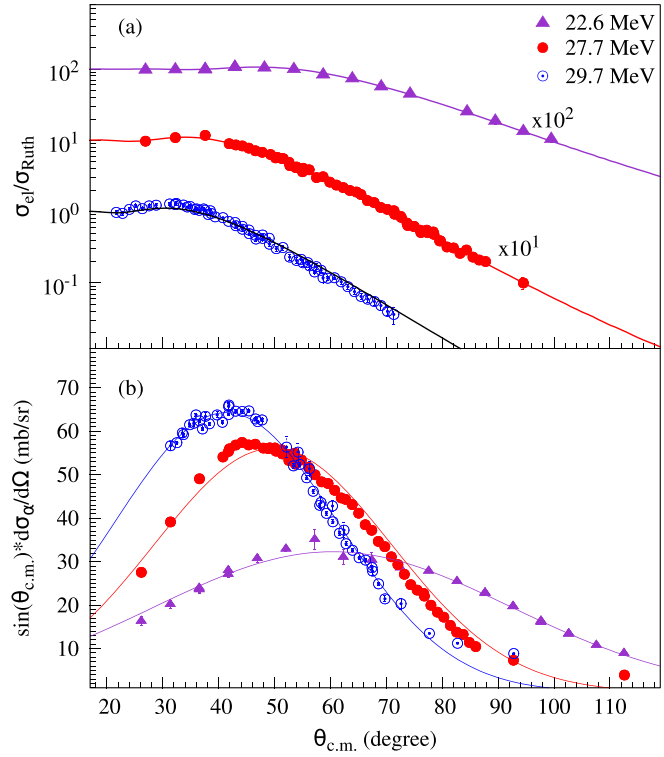

FIG. 4. The measured angular distributions of (a) elastic scattering and (b) inclusive α yield for the ^{7}Li + ^{89}Y system. The lines in (a) and (b) correspond to CDCC calculations and Gaussian fits, respectively.

In this type of measurements, the sources of systematic uncertainties are (a) thickness of the target, (b) fluctuation in beam current, (c) dead time of the acquisition system, and (d) angular position and solid angle of the detectors, etc. Uncertainties due to the above mentioned sources (a) to (c) were minimized by the absolute normalization method using monitor detectors, which were kept at ±20°. The uncertainties due to angle and solid angle of the detectors, which are estimated to be around 5–8%, were also minimized using elastic scattering measurements of ^{7}Li from ^{209}Bi and Monte Carlo simulations [15]. The uncertainties due to fitting of the angular distributions (2–4%) have also been included.

A. Elastic scattering and inclusive α

The measured elastic scattering angular distributions at the three energies for the ^{7}Li + ^{89}Y system are shown in Fig. 4(a). The errors on the data points are statistical only. The angular distributions of the inclusive α yield for the ^{7}Li + ^{89}Y system $[\frac{d\sigma}{d\Omega}(\theta_{\rm c.m.})\sin(\theta_{\rm c.m.})]$ are shown in Fig. 4(b) and are found to peak at the grazing angle. The angle integrated cross sections, given in Table I, were obtained by fitting the experimental angular distributions with Gaussian functions.

B. Prompt and resonant breakup of ^{7}Li

Resonant breakup occurs via an unbound resonant state having a finite width, which manifests itself as a well defined peak with same width in the relative energy spectrum, whereas prompt or continuum breakup, occurring via the nonresonant continuum, as the name suggests, leads to a continuous relative energy spectra. The peak at 2.16 MeV in the relative energy spectrum of the $\alpha + t$ coincidences as shown in Fig. 2(f) corresponds to the resonant breakup of ^{7}Li from its $\frac{7}{2}^-$ ($E^* = 4.63$ MeV) state. The measured relative energy distributions were fitted with a sum of Briet-Wigner form (for resonance) and a function $f(E_{\rm rel}) = aE_{\rm rel}^b e^{-(E_{\rm rel}-E_0)/d}$ (for the prompt contribution). The uncertainties in the extracted prompt and resonance contributions are estimated to be 5%, corresponding to the uncertainties in the fitted parameters. The angular distributions of the resonant and prompt breakup at $E_{\rm lab} = 27.7$ MeV for the ^{89}Y target are shown in Fig. 5. As can be seen from the figure, the angular distribution of the resonant breakup is found to peak around the grazing angle, whereas for the prompt breakup, no peak is observed in the measured angular range. The prompt breakup cross section is found to be smaller than the resonant breakup by an order of magnitude. The angle integrated cross sections along with the calculated values are listed in Table I. The calculated resonant breakup cross section increases with beam energy.

TABLE I. Comparison of cross sections for various reaction channels for the ^{7}Li + ^{89}Y and ^{7}Li + ^{93}Nb [11] systems. The results of CDCC calculations for ^{7}Li$^{*}(7/2^{-}) \rightarrow \alpha + t$ breakup and CCBA calculations for 1n-stripping and 1p-pickup and -stripping reactions are also given.

Channel	E^{*} (MeV)	σ_{exp} (mb)	σ_{cal} (mb)	σ_{exp} (mb)	σ_{cal} (mb)	σ_{exp} (mb)	σ_{cal} (mb)
^{7}Li + ^{89}Y		$E_{lab} = 22.6$ MeV		$E_{lab} = 27.7$ MeV		$E_{lab} = 29.7$ MeV	
α inclusive		280 ± 34		325 ± 40		354 ± 46	
^{8}Be$_{g.s.}(\alpha+\alpha)$ + ^{88}Sr*	g.s.	0.06 ± 0.02	0.07	0.08 ± 0.03	0.08	0.10 ± 0.03	0.10
	$E^{*} = 1.8$	0.28 ± 0.03	0.26	0.27 ± 0.03	0.29	0.28 ± 0.02	0.29
	$2.5 < E^{*} \leqslant 5$	1.2 ± 0.3	1.10	1.3 ± 0.3	1.15	1.3 ± 0.3	1.16
	$E^{*} \leqslant 15$	1.8 ± 0.2		1.9 ± 0.3		2.0 ± 0.3	
^{6}Li$^{*}_{3^{+}}(\alpha+d)$ + ^{90}Y*	$E^{*} \leqslant 1$	8.6 ± 0.8	6.4	9.8 ± 0.9	8.3	10.3 ± 1.0	9.1
	$E^{*} \leqslant 4$	9.3 ± 1.1	9.7	14.6 ± 1.3	15.2	15.6 ± 1.5	16.8
^{6}Li$_{g.s.}$ + ^{90}Y*	$E^{*} \leqslant 1$	14.2 ± 1.9	13.1	15.6 ± 1.4	15.8	16.1 ± 1.7	17.2
	$E^{*} \leqslant 4$	30.1 ± 2.4	27.4	33.4 ± 2.8	32.9	34.2 ± 3.1	34.9
^{7}Li$_{\frac{7}{2}^{-}}(\alpha+t)$ + ^{89}Y			1.51	3.5 ± 0.3	3.05		3.65
^{6}He$_{g.s.}$ + ^{90}Zr			2.9	7.8± 1.0	5.0	9.4 ± 1.2	5.9
Reaction			856		1252		1368
^{7}Li + ^{93}Nb		$E_{lab} = 23.6$ MeV		$E_{lab} = 27.7$ MeV		$E_{lab} = 29.7$ MeV	
α inclusive		273 ± 40		321 ± 48		340 ± 52	
^{8}Be$_{g.s.}(\alpha+\alpha)$ + ^{92}Zr*	$E^{*} \leqslant 3$	0.5 ± 0.1	0.36	0.7 ± 0.1	0.56	0.6 ± 0.1	0.53
	$E^{*} \leqslant 15$	1.5 ± 0.2		2.0 ± 0.3		2.3 ± 0.3	
^{6}Li$^{*}_{3^{+}}(\alpha+d)$ + ^{94}Nb	$E^{*} \leqslant 1$	5.2 ± 0.5	5.5	5.8 ± 0.4	6.2	6.2 ± 0.4	6.2
	$E^{*} \leqslant 4$	9.8 ± 1.1		13.8 ± 1.4		14.7 ± 1.4	
^{6}Li$_{g.s.}$ + ^{94}Nb	$E^{*} \leqslant 1$	9.9 ± 1.0	9.8	11.0 ± 1.2	10.9	11.2 ± 1.5	10.3
	$E^{*} \leqslant 4$	25.5 ± 3.2		32.2 ± 3.6		34.0 ± 3.3	
^{7}Li$_{\frac{7}{2}^{-}}(\alpha+t)$ + ^{93}Nb				3.3 ± 0.6	2.9		
^{6}He$_{g.s.}$ + ^{94}Mo			7.2 ± 0.9		8.6 ± 1.0		
Reaction			1121		1310		1489

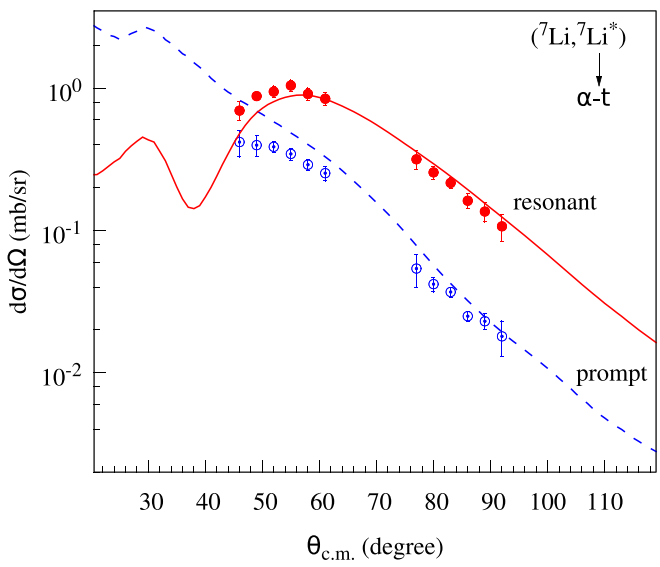

FIG. 5. The measured cross sections for prompt and resonant (from the $\frac{7}{2}^{-}$ state) breakup of ^{7}Li compared with CDCC calculations for the ^{89}Y target at $E_{lab} = 27.7$ MeV.

C. 1n-stripping ^{89}Y(^{7}Li, ^{6}Li*)^{90}Y* reaction

For the case of the 1n-stripping reaction, the cross sections for ^{6}Li breakup from the 3^{+}_{1} (2.18 MeV) state into $\alpha + d$ were extracted. As indicated in Fig. 3(b), there are many closely lying states in ^{90}Y which were not resolved in the present measurement. However, two distinct peaks are observed. The low energy peak is expected to be an admixture of the g.s. (2^{-}) and first excited state (3^{-}). The extracted absolute angular distributions shown in Figs. 6(a) and 6(b) correspond to the low energy peak ($E^{*} \leqslant 1.0$ MeV) and the full excitation range ($E^{*} \leqslant 4.0$ MeV), respectively. The integrated cross sections obtained from Gaussian fits to the angular distributions are listed in Table I.

A comparative study of the 1n-stripping reactions for ^{89}Y and ^{93}Nb targets is expected to be interesting, as the former has a closed neutron shell ($N = 50$) configuration and the latter has two extra neutrons outside this shell. Two important features may be noted from the data shown in Table I. The measured cross sections for 1n stripping leading to the ^{6}Li$_{g.s.}$ as well as ^{6}Li$_{3^{+}_{1}}$ for the ^{89}Y target are found to be about ≈1.5 times larger compared to those for ^{93}Nb for excitation of the target-like nuclei up to 1 MeV. However, the cross sections are found to be equal within the experimental uncertainties if the full range of excitation of the target-like nuclei is considered.

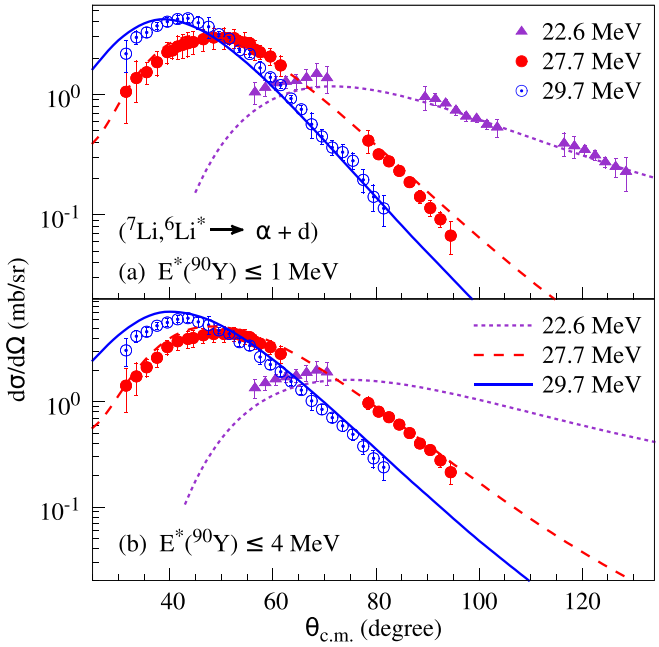

FIG. 6. Experimental absolute angular distributions of the $1n$-stripping ^{89}Y(^{7}Li, ^{6}Li*)^{90}Y* reaction at 22.6, 27.7, and 29.7 MeV for (a) $E^*(^{90}\mathrm{Y}) \leqslant 1$ MeV and (b) $E^*(^{90}\mathrm{Y}) \leqslant 4$ MeV compared with CCBA calculations.

D. $1p$-pickup and -stripping reactions

As shown in Fig. 3(a), several peaks are observed in the excitation energy spectra of ^{88}Sr populated via the $1p$-pickup reaction. The two low energy peaks are identified as the ground state and the first excited state of ^{88}Sr. The strongly populated peak at ≈3.5 MeV might have contributions from several states, which are discussed in Sec. IV. Angular distributions for $1p$ pickup corresponding to the first three peaks as discussed above are shown in Fig. 7. These angular distributions are from ^{8}Be ground state only. Although ^{89}Y has a proton hole and ^{93}Nb has an extra proton relative to the semimagic $Z = 40$ shell closure, the angle-integrated cross sections (E^*_{target} up to 15 MeV) are found to be similar for the two cases. The angular distributions for the $^6\mathrm{He}_{\mathrm{g.s.}}$ populated via the $1p$-stripping reaction were also extracted, and angle-integrated cross sections are tabulated in Table I. While the $1p$-stripping cross section $\sigma(^6\mathrm{He}_{\mathrm{g.s.}})$ is found to be larger than the $1p$-pickup cross section $\sigma(^8\mathrm{Be}_{\mathrm{g.s.}})$ by an order of magnitude, the total $1n$-stripping cross section $\sigma(^6\mathrm{Li}_{\mathrm{g.s.}}) + \sigma(^6\mathrm{Li}_{3^+})$ is found to be largest.

IV. COUPLED CHANNEL CALCULATIONS

The measured cross sections for different breakup processes as well as transfer channels leading to the ejectile in bound and unbound states are compared with coupled channel calculations using the code FRESCO [18]. The elastic scattering and breakup cross sections for ^{7}Li were calculated within the CDCC prescription using the cluster folding model. The angular distributions for the transfer-breakup processes, $1p$ pickup followed by breakup of $^8\mathrm{Be}(\rightarrow \alpha + \alpha)$ and $1n$ stripping followed by breakup of $^6\mathrm{Li}(\rightarrow \alpha + d)$, were obtained within the CCBA formalism employing potentials that describe the elastic scattering data, where available.

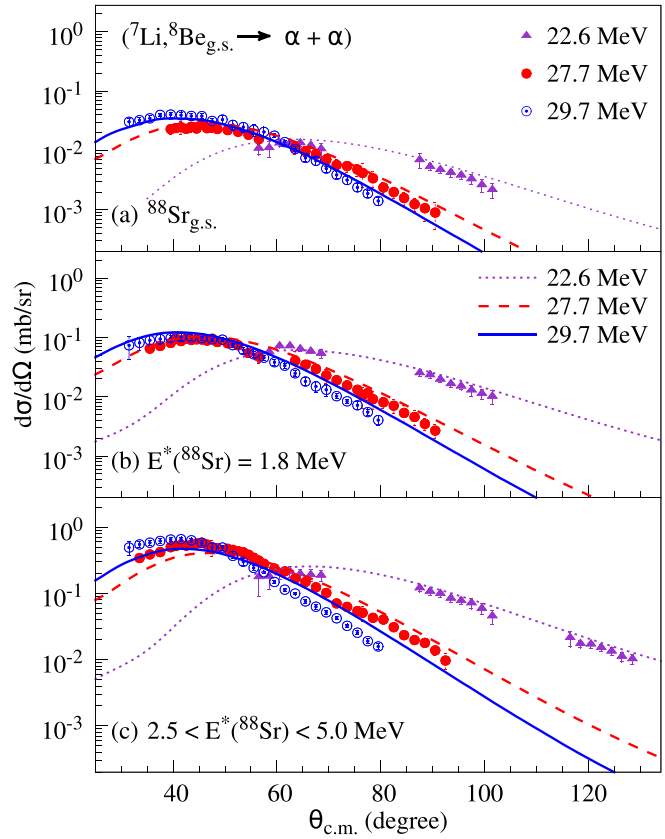

FIG. 7. Measured angular distributions of the ^{89}Y(^{7}Li, ^{8}Be)^{88}Sr* ($1p$-pickup) channel for (a) ground state, (b) first excited state, and (c) $2.5 \leqslant E^* \leqslant 5.0$ MeV of ^{88}Sr. CCBA calculations are represented by lines.

The $^7\mathrm{Li} \rightarrow \alpha + t$ breakup data were analyzed with CDCC calculations, similar to those described in Refs. [11,19]. The ^{7}Li continuum was divided into discrete bins in momentum (k) space of width $\Delta k = 0.1$ fm^{-1} with $k_{\mathrm{max}} = 0.8$ fm^{-1}. Relative angular momenta of $L = 0$–4 between the clusters and couplings up to multipolarity $\lambda = 4$ were included in the calculations. The $\alpha + ^{89}$Y and $t + ^{89}$Y optical potentials required as input to the Watanabe-type folding potentials were taken from the global parametrizations of Refs. [20] and [21], respectively. The best fits to the elastic scattering data, shown in Fig. 4, were obtained by normalizing the depths of the real and the imaginary potentials by factors of 0.6 and 0.8, respectively. The extracted reaction cross sections are given in Table I. The calculated angular distributions for both the prompt and resonant breakup of ^{7}Li (Fig. 5) are in good agreement with the experimental observations.

The channels of $1n$ stripping followed by breakup of ^{6}Li ($\rightarrow \alpha + d$) were analyzed within the CCBA formalism. In addition to the ^{89}Y(^{7}Li, ^{6}Li*)^{90}Y* transfer couplings, inelastic excitations of the $^7\mathrm{Li}(1/2^-)$ and the $^6\mathrm{Li}(3^+_1)$ excited states were included in the entrance and exit partitions, respectively. The entrance channel optical potentials were based on the

global ^{7}Li parameters of Ref. [22] with real and imaginary depths adjusted to fit the elastic scattering data after the inclusion of the ^{7}Li couplings. The $3/2^{-}$(g.s.) and $1/2^{-}$(0.478 MeV) states of ^{7}Li were treated as members of a $K = 1/2$ rotational band. The $B(E2; 3/2^{-} \rightarrow 1/2^{-})$ value was taken from Ref. [23] and the nuclear deformation length of $\delta_2 = 2.4$ fm was obtained by fitting the inelastic scattering data of Ref. [24]. The $B(E2; 1_1^{+} \rightarrow 3_1^{+})$ value for ^{6}Li was taken from Ref. [25] and the nuclear deformation length of $\delta_2 = 1.9$ fm was obtained by fitting the sequential breakup data of Ref. [26]. The 1_1^{+} and 3_1^{+} states of ^{6}Li were assumed to be members of a $K = 1$ rotational band, with the exception that reorientation of the 1_1^{+} ground state was omitted due to the very small quadrupole moment of this state. The exit channel optical potentials employed the ^{6}Li global parameters of Ref. [22] with real and imaginary well depths adjusted to match elastic scattering angular distributions. Spectroscopic factors for $\langle {}^{7}\mathrm{Li} | {}^{6}\mathrm{Li} + n \rangle$ and $\langle {}^{90}\mathrm{Y} | {}^{89}\mathrm{Y} + n \rangle$ overlaps were taken from Refs. [27] and [28], respectively. In addition to transfers from the ground state and $1/2^{-}$ state of ^{7}Li to the 1_1^{+} and 3_1^{+} states of ^{6}Li, the following ^{90}Y states were included: 2^{-} (g.s.), 3^{-} (0.203 MeV), 0^{-} (1.22 MeV), 1^{-} (1.38 MeV), 5^{+} (1.962 MeV), 6^{+} (2.25 MeV), 2^{-} (2.48 MeV), 1^{-} (2.63 MeV), 4^{-} (2.94 MeV), and 3^{-} (3.05 MeV). The cumulative angular distributions for the first two ^{90}Y states (g.s. and 3^{-}) and the remaining states reproduce reasonably well the corresponding measured distributions as shown in Figs. 6(a) and 6(b), respectively.

Similar CCBA calculations were performed for the $\alpha - \alpha$ coincidence data considering the ^{89}Y(^{7}Li, ^{8}Be)^{88}Sr* $1p$-pickup processes. The entrance channel potentials were the same as those described above. Since ^{8}Be optical potentials are not available due to its unbound nature, ^{7}Li global parameters [22] were used in the exit channel. Pickup to the ground state of ^{8}Be and the 0^{+} (g.s.), 2^{+} (1.836 MeV), 2^{+} (3.22 MeV), 1^{+} (3.49 MeV) and 2^{+} (3.63 MeV) states of ^{88}Sr were included, representing the complete set of states for which the relevant spectroscopic factors are available. The spectroscopic factors for the $\langle {}^{8}\mathrm{Be} | {}^{7}\mathrm{Li} + p \rangle$ and $\langle {}^{89}\mathrm{Y} | {}^{88}\mathrm{Sr} + p \rangle$ overlaps were taken from Refs. [27] and [29] (Set I), respectively. The calculated 0^{+} (g.s.) cross sections are normalized by a factor of 0.35 to get a better agreement with the data. The calculated 0^{+} (g.s.) and 2^{+} (1.84 MeV) cross sections are shown in Figs. 7(a) and 7(b), respectively. The cumulative cross sections for the 2^{+} (3.22 MeV), 1^{+} (3.49 MeV) and 2^{+} (3.63 MeV) states are compared with the data in Fig. 7(c). All the measured $1p$-pickup angular distributions are well reproduced.

The cross sections for the ^{89}Y(^{7}Li, ^{6}He$_{\mathrm{g.s.}}$)^{90}Zr stripping process were also estimated via similar CCBA calculations. The entrance and exit channel potentials were treated identically to the CCBA calculations for the $1n$-stripping reaction. The $\langle {}^{90}\mathrm{Zr} \mid {}^{89}\mathrm{Y} + p \rangle$ and $\langle {}^{7}\mathrm{Li} \mid {}^{6}\mathrm{He} + p \rangle$ overlaps were taken from Refs. [30] and [31], respectively. The calculated cross sections corresponding to excitation energy of ^{90}Zr up to 8 MeV are listed in Table I. As the spectroscopic factors for the $\langle {}^{94}\mathrm{Mo} \mid {}^{93}\mathrm{Nb} + p \rangle$ overlap are available only up to 3 MeV [32], similar calculations were not performed for the ^{93}Nb target.

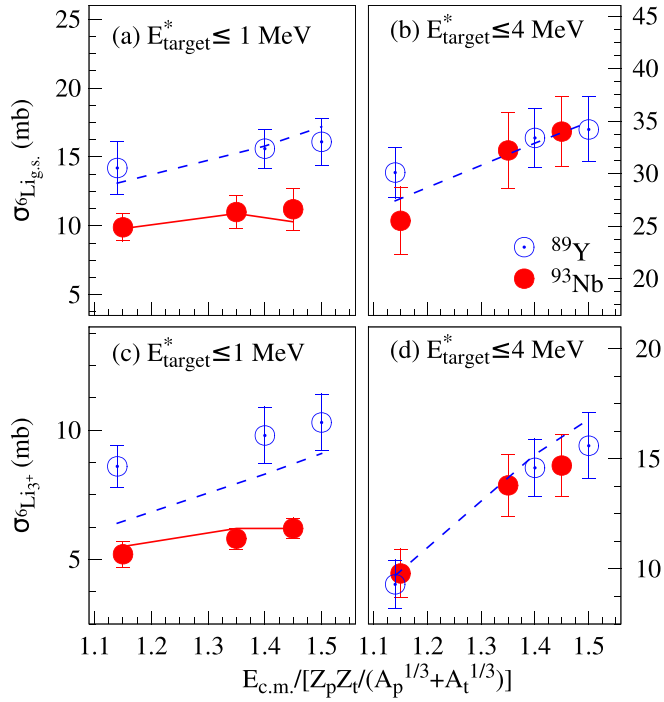

FIG. 8. The cross sections of $1n$ stripping leading to ^{6}Li(g.s.) and ^{6}Li(3^{+}), respectively, for ^{7}Li induced reactions with ^{89}Y and ^{93}Nb targets are compared. The cross sections corresponding to the ranges of excitation energy of target-like nuclei $E^{*} \leqslant 1$ MeV and $E^{*} \leqslant 4$ MeV are presented in (a),(c) and (b),(d), respectively. The dashed and solid lines represent the results of CCBA calculations for ^{89}Y and ^{93}Nb targets, respectively.

Observed variance between the calculated and the measured cross sections for the various processes are within expectations, given the inevitable uncertainties in some of the input parameters. Hence, the overall description of the data can be considered as reasonable.

V. DISCUSSION

In this section, we discuss the role of target structure in direct reactions. The $1n$-stripping cross sections for ^{89}Y and ^{93}Nb targets are compared in Fig. 8 as a function of the reduced energy, $E_{\mathrm{c.m.}}/[Z_p Z_t/(A_p{}^{1/3} + A_t{}^{1/3})]$, where $E_{\mathrm{c.m.}}$ is the energy in the center-of-mass frame. The atomic and mass numbers of the projectile (target) are denoted by Z_p (Z_t) and A_p (A_t), respectively. The cross sections for target excitation energies up to 1 MeV, corresponding to the first distinct peak in the spectra shown in Figs. 3(b) and 3(e), are found to be 1.5 times larger for ^{89}Y than for ^{93}Nb, irrespective of the ejectile excitation (^{6}Li, g.s. and 3^{+} state) and bombarding energies (left panels). However, the cross sections are found to be similar if the excitation energy range up to 4 MeV, corresponding to essentially all of the observed strength, is considered (right panels). These observations may be understood using the semiclassical theory [16,17]. For both targets the valence orbital involved for neutron transfer is $d_{5/2}$ and the kinematical matching conditions (optimum Q value

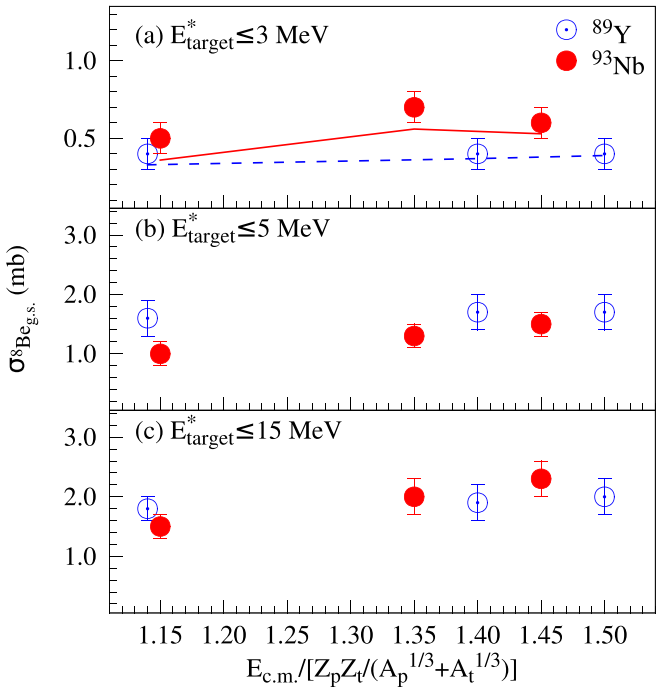

FIG. 9. The cross sections of $1p$ pickup leading to the ^{8}Be$_{g.s.}$ for both the ^{89}Y and ^{93}Nb targets for three different excitation energy ranges of the target-like nuclei as labeled in the figure. The CCBA calculations are shown in dashed and solid lines for ^{89}Y and ^{93}Nb targets, respectively.

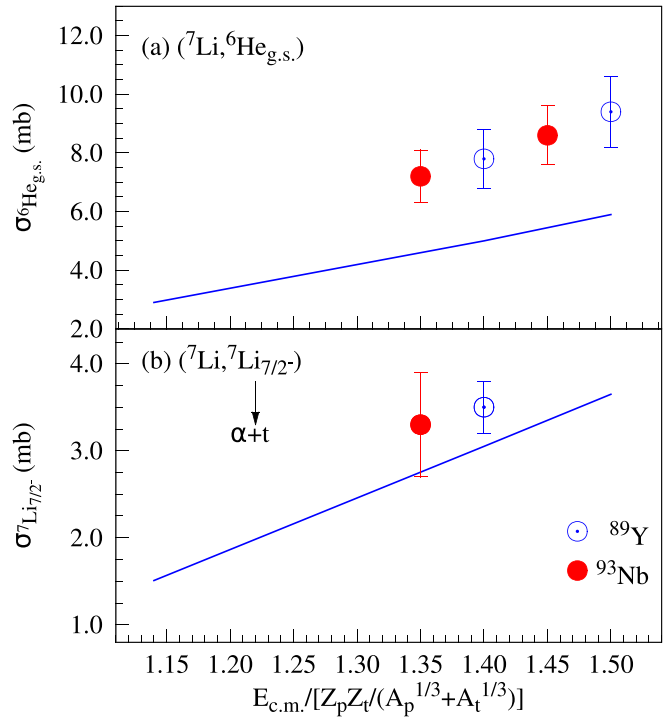

FIG. 10. The measured angle integrated cross sections of (a) the $1p$ stripping leading to ^{6}He$_{g.s.}$ and (b) direct breakup of ^{7}Li for ^{89}Y and ^{93}Nb targets are compared. The line represents the calculations for the ^{7}Li + ^{89}Y system.

and angular momentum) are the same. However, the smaller fragmentation of the single-particle strength in ^{90}Y than in ^{94}Nb leads to larger cross sections for the former if only target excitation up to 1 MeV is considered, since more of this strength is concentrated in the first peak for ^{90}Y. The observed ratio (1.5) of cross sections for low target excitations (⩽1 MeV) may also be correlated to the ratio of vacancies (1.5) as there are 6 (4) vacancies in the $d_{5/2}$ orbital of ^{89}Y (^{93}Nb). The observed equivalence of the $1n$-stripping cross sections for the two targets when the whole excitation range is considered suggests that the total single-particle strengths in the residual nuclei are similar. The above observations concerning the strength for target excitation up to 1 MeV are reproduced by the CCBA calculations. In Figs. 8(b) and 8(d), only calculations for the ^{7}Li + ^{89}Y system are shown, since information on the spectroscopic factors for ^{94}Nb is only available up to an excitation energy of 2.32 MeV [33], which does not represent a convenient cutoff point in the relevant spectrum. An excitation energy range of $0.0 \leqslant E^* \leqslant 1$ MeV was chosen for detailed comparisons between theory and experiment and between the two targets since this represents a convenient cut-off point in the spectrum for both systems; see Figs. 3(b) and 3(e).

We also have investigated whether the $1p$-pickup and -stripping reactions behave in a similar way. Since ^{93}Nb has one extra proton and ^{89}Y has a proton hole with respect to the $Z = 40$ subshell closure, intuitively one would expect the cross sections for proton transfer to be different for these two targets. Although the cross sections for $1p$ pickup are found to be slightly larger for ^{93}Nb compared to ^{89}Y for $E^* \leqslant 3$ MeV, they are similar when a larger range of target excitation energy is considered (Fig. 9). In this case, the kinematical matching conditions are also the same for these two targets. However, large mismatches between the Q_{gg} and Q_{opt} hinder the population of states near the ground state, making the total cross sections insensitive to the target structure since they favor pickup from more deeply bound levels which are filled in both nuclei. Similarly, the $1p$-stripping cross sections are found to be the same within the experimental uncertainty for these targets, as shown in Fig. 10(a), due to the large values of $Q_{gg} - Q_{opt}$, favoring population of higher-lying levels that are vacant in both nuclei. The CCBA calculations reproduce these trends for the $1p$-pickup reactions for excitation ⩽3 MeV; see Fig. 9(a). While 3 MeV represents a convenient cutoff in the ^{88}Sr spectrum, there is no such situation in the corresponding ^{92}Zr spectrum; see Figs. 3(a) and 3(d). Rather, it represents the maximum excitation energy for which relevant spectroscopic information is available in ^{92}Zr; see Ref. [11].

The measured cross sections for ^{7}Li breakup via the $\frac{7}{2}^-$ state for these two targets are compared in Fig. 10(b). The cross sections are found to be similar and follow the expected trends predicted by the CDCC calculations. In this case, the similar orders of the Coulomb and nuclear fields experienced by the ^{7}Li projectile interacting with either target is the reason for the similar cross sections at similar reduced energies, since the target is essentially a spectator in the breakup process.

VI. SUMMARY AND CONCLUSION

In summary, the present work reports a detailed quantitative study of the role of target structure in different reaction mechanisms, viz., direct breakup, $1p$ transfer, and $1n$ stripping leading to bound and unbound states of the ejectile at collision energies near the Coulomb barrier. The exclusive absolute cross sections were measured for various reaction channels. Calculations were performed using the CDCC and CCBA formalisms to understand the comprehensive data set comprising elastic scattering, transfer, direct breakup, and transfer breakup. The measured cross sections for the (^{7}Li, ^{6}Li$_{\text{g.s.}}$) and (^{7}Li, ^{6}Li$_{3^+_1}$) $1n$-stripping reactions for the ^{89}Y target are found to be about $\approx$1.5 times larger than those for the ^{93}Nb target for excitation energies up to 1 MeV. However, the integrated cross sections are found to be similar for target excitation up to 4 MeV. In addition to the kinematic matching conditions (optimum Q value and angular momentum), a correlation is also observed between the vacancies in the valence orbital of the target nucleus and the measured stripping cross sections for low-energy target excitation. In the case of $1p$-pickup and -stripping reactions the mismatch between Q_{gg} and Q_{opt} is large, leading to more population around $E^* = Q_{\text{gg}} - Q_{\text{opt}}$ than the ground state for both targets. Consequently, the measured cross sections are found to be insensitive to the target structure. Further investigation in this direction probing the effect of target structure on reactions involving other weakly bound stable (e.g., ^{6}Li, ^{9}Be) and unstable projectiles will enrich the field.

ACKNOWLEDGMENTS

We thank the Mumbai BARC-TIFR Pelletron-Linac accelerator staff for providing steady and uninterrupted beam and P. Patale for help during the experiment.

[1] M. Dasgupta, D. J. Hinde, N. Rowley, and A. M. Stefanini, Annu. Rev. Nucl. Part. Sci. **48**, 401 (1998).
[2] J. J. Kolata, V. Guimarães, and E. F. Aguilera, Eur. Phys. J. A **52**, 123 (2016).
[3] L. F. Canto, P. R. S. Gomes, R. Donangelo, J. Lubian, and M. Hussein, Phys. Rep. **596**, 1 (2015).
[4] N. Keeley, N. Alamanos, K. W. Kemper, and K. Rusek, Prog. Part. Nucl. Phys. **63**, 396 (2009).
[5] C. Signorini, A. Edifizi, M. Mazzocco, M. Lunardon, D. Fabris, A. Vitturi, P. Scopel, F. Soramel, L. Stroe, G. Prete, E. Fioretto, M. Cinausero, M. Trotta, A. Brondi, R. Moro, G. La Rana, E. Vardaci, A. Ordine, G. Inglima, M. La Commara, D. Pierroutsakou, M. Romoli, M. Sandoli, A. Diaz-Torres, I. J. Thompson, and Z. H. Liu, Phys. Rev. C **67**, 044607 (2003).
[6] A. Shrivastava, A. Navin, N. Keeley, K. Mahata, K. Ramachandran, V. Nanal, V. V. Parkar, A. Chatterjee, and S. Kailas, Phys. Lett. B **633**, 463 (2006).
[7] A. Pakou, N. Alamanos, N. Clarke, N. Davis, G. Doukelis, G. Kalyva, M. Kokkoris, A. Lagoyannis, T. Mertzimekis, A. Musumarra, N. Nicolis, C. Papachristodoulou, N. Patronis, G. Perdikakis, D. Pierroutsakou, D. Roubos, K. Rusek, S. Spyrou, and C. Zarkadas, Phys. Lett. B **633**, 691 (2006).
[8] S. Santra, V. V. Parkar, K. Ramachandran, U. K. Pal, A. Shrivastava, B. J. Roy, B. K. Nayak, A. Chatterjee, R. K. Choudhury, and S. Kailas, Phys. Lett. B **677**, 139 (2009).
[9] F. Souza, C. Beck, N. Carlin, N. Keeley, R. L. Neto, M. de Moura, M. Munhoz, M. D. Santo, A. Suaide, E. Szanto, and A. S. de Toledo, Nucl. Phys. A **821**, 36 (2009).
[10] D. Martinez Heimann, A. J. Pacheco, O. A. Capurro, A. Arazi, C. Balpardo, M. A. Cardona, P. F. F. Carnelli, E. de Barbará, J. O. Fernández Niello, J. M. Figueira, D. Hojman, G. V. Martí, A. E. Negri, and D. Rodrígues, Phys. Rev. C **89**, 014615 (2014).
[11] S. K. Pandit, A. Shrivastava, K. Mahata, N. Keeley, V. V. Parkar, P. C. Rout, K. Ramachandran, I. Martel, C. S. Palshetkar, A. Kumar, A. Chatterjee, and S. Kailas, Phys. Rev. C **93**, 061602(R) (2016).
[12] S. K. Pandit, A. Shrivastava, K. Mahata, V. V. Parkar, R. Palit, N. Keeley, P. C. Rout, A. Kumar, K. Ramachandran, S. Bhattacharyya, V. Nanal, C. S. Palshetkar, T. N. Nag, S. Gupta, S. Biswas, S. Saha, J. Sethi, P. Singh, A. Chatterjee, and S. Kailas, Phys. Rev. C **96**, 044616 (2017).
[13] D. Chattopadhyay, S. Santra, A. Pal, A. Kundu, K. Ramachandran, R. Tripathi, D. Sarkar, S. Sodaye, B. K. Nayak, A. Saxena, and S. Kailas, Phys. Rev. C **94**, 061602(R) (2016).
[14] D. Chattopadhyay, S. Santra, A. Pal, A. Kundu, K. Ramachandran, R. Tripathi, B. J. Roy, T. N. Nag, Y. Sawant, B. K. Nayak, A. Saxena, and S. Kailas, Phys. Rev. C **97**, 051601(R) (2018).
[15] S. K. Pandit, K. Mahata, A. Shrivastava, V. V. Parkar, and K. Ramachandran, J. Instrum. **14**, T01005 (2019).
[16] D. Brink, Phys. Lett. B **40**, 37 (1972).
[17] J. L. C. Ford, K. S. Toth, G. R. Satchler, D. C. Hensley, L. W. Owen, R. M. DeVries, R. M. Gaedke, P. J. Riley, and S. T. Thornton, Phys. Rev. C **10**, 1429 (1974).
[18] I. J. Thompson, Comput. Phys. Rep. **7**, 167 (1988).
[19] C. Beck, N. Keeley, and A. Diaz-Torres, Phys. Rev. C **75**, 054605 (2007).
[20] V. Avrigeanu, P. E. Hodgson, and M. Avrigeanu, Phys. Rev. C **49**, 2136 (1994).
[21] J. F. D. Becchetti and G. W. Greenlees, *Polarization Phenomena in Nuclear Reactions* (The University of Wisconsin Press, Madison, 1971), p. 682.
[22] J. Cook, Nucl. Phys. A **388**, 153 (1982).
[23] A. Weller, P. Egelhof, R. Čaplar, O. Karban, D. Krämer, K.-H. Möbius, Z. Moroz, K. Rusek, E. Steffens, G. Tungate, K. Blatt, I. Koenig, and D. Fick, Phys. Rev. Lett. **55**, 480 (1985).
[24] R. Puigh and K. Kemper, Nucl. Phys. A **313**, 363 (1979).
[25] F. Ajzenberg-Selove, Nucl. Phys. A **490**, 1 (1988).
[26] S. P. Van Verst, D. P. Sanderson, K. W. Kemper, D. Shapira, R. L. Varner, and B. Shivakumar, Phys. Rev. C **36**, 1865 (1987).
[27] S. Cohen and D. Kurath, Nucl. Phys. A **101**, 1 (1967).
[28] R. E. Goans and C. R. Bingham, Phys. Rev. C **5**, 914 (1972).
[29] R. Wadsworth, M. D. Cohler, M. J. Smithson, D. L. Watson, F. Jundt, L. Kraus, I. Linck, and J. C. Sens, J. Phys. G: Nucl. Phys. **9**, 1237 (1983).
[30] G. Vourvopoulos and J. D. Fox, Phys. Rev. **177**, 1558 (1969).
[31] O. F. Nemets *et al.*, *Nucleon Clusters in Atomic Nuclei and Many-Nucleon Transfer Reactions* (Ukrainian Academy of Sciences, Kiev, 1988).
[32] M. R. Cates, J. B. Ball, and E. Newman, Phys. Rev. **187**, 1682 (1969).
[33] J. B. Moorhead and R. A. Moyer, Phys. Rev. **184**, 1205 (1969).